ACS OMEGA

Open Access

http://pubs.acs.org/journal/acsodf

Article

Synthesis and Capacitive Properties of Mesoporous Tungsten Oxide Films Prepared by Ultrasonic Spray Deposition

Chi-Ping Li* and Gui Yang Lai

Cite This: *ACS Omega* 2023, 8, 40878−40889

Read Online

ACCESS | Metrics & More | Article Recommendations

ABSTRACT: Mesoporous tungsten trioxide (WO_3) films are prepared by the combination of the template-assisted sol−gel method and ultrasonic spraying deposition (USD) for supercapacitors, and then the surface morphology and electrochemical performance of the films are studied. Compared to WO_3 prepared by the traditional hydrothermal synthesis and spin coating method, the films obtained by USD exhibit advantages such as low cost, minimal material usage, and suitability for large-area in-line manufacturing. Additionally, the mesoporous structure of USD-produced films is also supportive of ion transportation. Due to the high specific surface area of WO_3 films deposited by USD, it is a material capable of use in a high-performance energy storage device. Through the control of spray coats, the film thickness and specific capacitance can be effectively controlled. Electrochemical measurements show that the mesoporous WO_3 films possess excellent electrochemical performance with a maximum specific capacitance of 109.15 F/g at 0.5 A/g. The cycling performance up to 5000 cycles of mesoporous WO_3 films is due to the stable nature of nanocrystalline produced by the combination of USD and sol−gel chemistry.

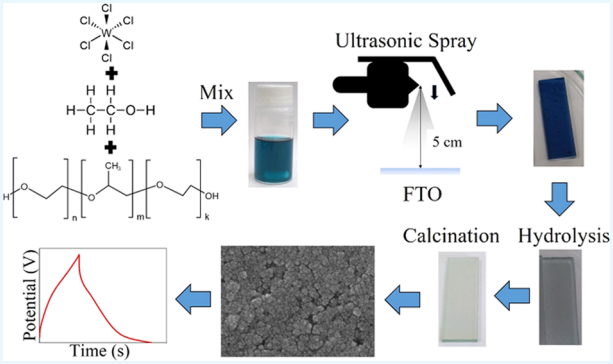

1. INTRODUCTION

The widespread popularity of electric vehicles and various portable and wearable electronic products has stimulated the demand for high-performance energy storage. Supercapacitors are promising energy storage devices, which are mainly divided into two types, electrochemical double-layer capacitors (EDLCs) and pseudocapacitors. The capacitance of a supercapacitor depends largely on the electrode materials. Generally, the materials used in supercapacitors are carbon materials, conductive polymers, and metal oxides. In order to achieve high specific surface area and produce high capacitance, carbon materials are usually used in electric double-layer capacitors (EDLCs), and the most popular material is activated carbon,[1−4] or based on this to develop materials with different shapes, such as carbon nanotubes,[5,6] graphene,[7,8] carbon onion,[9,10] aerogel,[11] xerogel,[12] templated carbon,[13,14] carbide-derived carbons (CDCs),[12−17] and so on.

Carbon materials have high specific surface areas, electrochemical stability, and unique electrical, chemical, thermal, and mechanical properties. However, their relatively high resistivity limits the performance of carbon materials as supercapacitor electrodes. Conductive polymers also have various advantages as electrode materials in supercapacitors. However, due to the intercalation/deintercalation of ions in redox reactions, conductive polymers are prone to expansion and contraction, resulting in mechanical degradation of electrode materials.[18] The materials of metal oxides are mainly transition metal oxides, such as RuO_2, IrO_2, MnO_2, NiO, SnO_2, and V_2O_5. The power density of metal oxides is higher than that of EDLC materials. Among all metal oxides, the most representative is RuO_2, which has been widely studied.[19−22] Because Ru itself is a noble metal, its cost is high and it is easy to pollute the environment, which limits its commercial application. Considering the cost and environmental issues, WO_3 is used in this study as the electrode of the supercapacitor. According to the literature,[23−26] WO_3 itself has unique characteristics, such as good electrochemical stability, low cost, high conductivity, and no pollution, and exhibits great potential as a material for supercapacitors. The electrochromic and energy storage capacities, as the advantage of tungsten trioxide, have attracted much attention and expectations for transparent wearable devices recently.[27,28]

In most studies, the hydrothermal method is used to synthesize metal oxides. However, it requires a high-temperature and high-pressure environment. The template-assisted gel−sol method[29−31] has been widely used to form

Received: August 16, 2023
Accepted: September 29, 2023
Published: October 16, 2023

Scheme 1. Schematic Diagram of the Mesoporous WO_3 Film Preparation

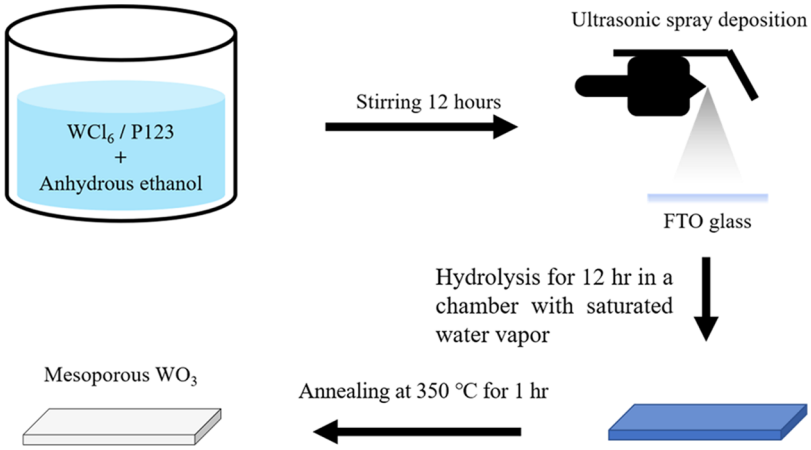

mesoporous metal oxide. This technique was introduced in this study and demonstrated as a better technique because it was operated at room temperature and atmospheric pressure. The deposition technique used in this study is ultrasonic spray deposition (USD). The material deposited on the FTO substrate using USD[32,33] is compared with that using the spin coating method in most literature.[34,35] Although the spin coating method is a convenient laboratory technique, it is not suitable for large-scale manufacturing. In addition, the dip coating method is another approach to preparing films.[36,37] However, the thickness of the upper and lower parts of the coated object produced by this process is uneven, and the solvent volatilization is large. Other methods such as chemical vapor deposition,[38] sputtering,[39,40] and electrodeposition[41−45] either require high vacuum or some special processing equipment, which leads to high capital. However, the USD can be controlled by a computer with repeatability and can be easily adjusted via various parameters that are used to precisely control the film thickness, such as spraying rate, spraying times, etc. It has the advantages of low cost, large-area coating, and the capability of in-line mass manufacturing. Our goal is to examine the capacitance of mesoporous tungsten trioxide (WO_3) films deposited by USD for use in wearable devices. The innovation of this work is the combination of USD, which is a low-cost and suitable process for scalable in-line production, and template-assisted sol−gel chemistry to synthesize mesoporous WO_3 with favorable capacitance. The superior energy storage capacity of mesoporous WO_3 films and the promising USD method are very competitive and can be used to replace the leading products and techniques in the market.

2. EXPERIMENTAL SECTION

2.1. Preparation of Sol Solution. Since the reagent is sensitive to moisture, the sol solution preparation needs to be carried out in a low-moisture environment. Poly(ethylene oxide)-poly(propylene oxide)-poly(ethylene oxide) (1.5 g, P123, Sigma-Aldrich) was weighed in a glove bag with moisture less than 30%. P123 was dissolved in 10 mL of absolute ethanol (≥99.5%) and stirred with a magnet for 30 min until P123 was completely dissolved. Then, 892.5 mg of tungsten hexachloride (WCl_6) (≥99.9%, Acros Organics) was added. After the sol was stirred for 12 h, it was transferred into an injection syringe and mounted on an ultrasonic spraying system.

2.2. Preparation of Gel and Tungsten Trioxide Films. Before spraying, the FTO glass (TEC-15, Pilkington, 20 Ω/□) was cleaned with alcohol, acetone, deionized water, and isopropanol through an ultrasonic oscillator for 3 min each and placed in the spraying area under the spray nozzle. After 12 h stir, the sol was transferred into an injection syringe and a liquid flow injection pump (brand: YSC, model: SP series) was used to send the sol into the ultrasonic spraying nozzle at a flow rate of 0.25 mL/min. The ultrasonic spraying system is mainly composed of a table-type ultrasonic spraying machine (brand: Dispensing Technology, model: DT-300), ultrasonic spray nozzle (brand: Sono-Tek, frequency: 120 kHz), and ultrasonic spraying controller (brand: Sono-Tek). In addition, it is also equipped with a gas delivery system with a gas flow controller (brand: Cylinder World), which can carry the atomized sol in a nitrogen flow with a flow rate of 6.9 slm down to the FTO glass. The vibration frequency of the nozzle was adjusted to 120 kHz with a power of 4 W. Through the computer-controlled nozzle, the WO_3 sol was sprayed back and forth evenly on the FTO glass 5 cm below the nozzle at a speed of 3.8 cm/s. After the FTO glass was sprayed, an iridescent blue film was formed on the surface. Then, the sprayed sample was placed in a container filled with water vapor for hydrolysis. The final step was calcination. The sample was hydrolyzed for 12 h on a hot plate maintained at 350 °C in the air for 1 h. The purpose is to remove the P123 and complete WO_3 oxidation and crystallization at the same time. After calcination, the sample was taken out and cooled to room temperature in the air. Scheme 1 presents a schematic diagram of the mesoporous WO_3 film preparation process.

2.3. Characterization of Deposited Tungsten Trioxide Films. The crystallinity of the films was characterized by X-ray diffraction (XRD) using a Cu K target, scanned over a range of 2θ = 20−65° using 0.05° per step. Raman spectroscopy was carried out using a 488 nm line of a 15 mW argon ion laser. Nitrogen physisorption was executed using Micrometrics ASAP 2020 after the samples were degassed at 250 °C under a vacuum for 4 h. The nanoscale characterization was inspected by transmission electron microscopy (TEM, Philips FEI CM200). X-ray photoelectron spectroscopy (XPS) was employed to examine the tungsten oxide films. A Kratos system with an Al Kα X-ray source was used. The base pressure of the analysis chamber was less than 10^{-9} Torr, and high-resolution spectra of individual binding states were recorded using a sweep time of 60 s at a pass voltage of 40

https://doi.org/10.1021/acsomega.3c05677
ACS Omega 2023, 8, 40878−40889

eV. The surface morphology of the film was carried out by scanning electron microscopy (JSM-5600). Fourier transform infrared (FTIR) (Thermo 6700 FTIR spectrometer) was introduced to obtain the FTIR spectra by mixing the powder of tungsten oxide with the KBr powder. By placing the sample in 1 M $LiClO_4$/PC electrolyte (the reference electrode is saturated Ag/AgCl, and the counter electrode is a Pt wire), the potentiostat (brand: Biologic, model SP-150) and the electrochemical measurements were performed at room temperature in the atmosphere.

3. RESULTS AND DISCUSSION

3.1. Surface Morphology of Mesoporous Tungsten Oxide Thin Film. Figure 1 shows the SEM image of the magnified surface morphology and structure of the prepared tungsten trioxide. It can be found that the tungsten trioxide coating on the FTO electrode has mesoporous structures and the film consists of tungsten oxide nanocrystallites.[46] The mesoporous structure is due to the addition of P123 as a template. The use of different hydrophilic and hydrophobic properties between polymer chains, which are incompatible with each other, results in microscopic phase separation (microphase separation).[47] Then, P123 is oxidized and removed during calcination to produce a mesoporous structure. Thus, through field emission scanning electron microscopy (FE-SEM), tungsten trioxide molecules form a large number of nanometer-scale mesoporous structures on the FTO conductive glass.

3.2. Structural Characterization of Mesoporous Tungsten Oxide Thin Film. The WO_3 film obtained using USD and template-assisted sol−gel method demonstrated a monoclinic phase from XRD (Figure 2) and Raman (Figure 3) characterizations. The XRD pattern showed crystalline features of both the monoclinic (I) γ-phase (JCPDS 43−1035) and the monoclinic (II) ε-phase (JCPDS 87−2402), a result that is consistent with previous reports.[48,49] The Raman spectrum also agrees with the XRD result that indicated a monoclinic phase,[50−52] including peaks around 267, 717, and 809 cm^{-1} for the γ-monoclinic phase and around 640 and 679 cm^{-1} in the shoulder for the ε-monoclinic phase. The broad and relatively weak peaks in XRD are attributed to the mesoporous nature of the films, which disrupts long-range order.[33]

Figure 4a is the transmission electron microscopy (TEM, FEI CM200) image, and Figure 4b is the selected electron area diffraction (SEAD) patterns obtained from tungsten trioxide films. The nanocrystalline nature of WO_3 is confirmed by TEM imaging. The lattice spacing of 0.37 nm and the indexing of the associated SEAD patterns indicate that WO_3 is present as the monoclinic γ-phase, which agrees with XRD and Raman characterization.[46]

X-ray photoelectron spectroscopy (XPS) was used to study the chemical composition and W oxidation states of the WO_3 films. Figure 5 shows the XPS W 4f spectra of the tungsten oxide thin films. The peaks at 36.3 and 38.1 eV are assigned to W^{6+}, while those at 34.5 and 37.2 eV are assigned to W^{5+}.[53,54] Moreover, W^{5+} is considered the linear combination product of W^{6+} with a lower W valence state or related to oxygen vacancies in WO_3.[55]

Figure 6 shows the FTIR spectra obtained from the WO_3 films and P123. The most significant peak of P123 is the C−H stretching signal around 2980−2850 cm^{-1}, and these features are completely removed after annealing of the film.[55] The signal around 1760−1690 cm^{-1} is due to the formation of carbonate (C═O) impurities in the process of decomposition. The hydroxyl groups show a broad feature between 3200 and 3700 cm^{-1}. This impurity may come from either incomplete annealing or adsorption from ambient in the experiment.[56] The feature in the low wavenumber around 600−1000 cm^{-1} is due to the O−W−O stretching, which has three modes at 642,

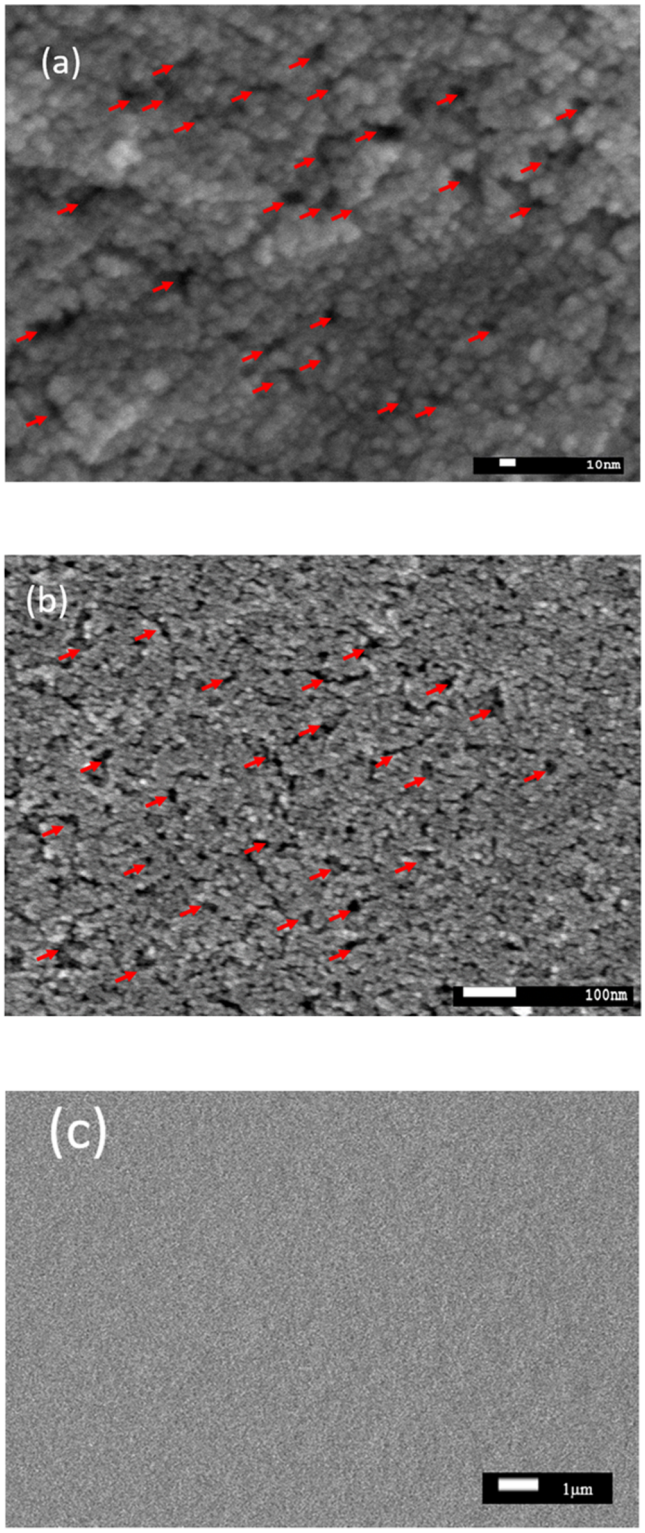

Figure 1. Surface morphology of mesoporous (red arrows) tungsten oxide from SEM under (a) 300,000×, (b) 100,000×, and (c) 5000× magnifications.

https://doi.org/10.1021/acsomega.3c05677
ACS Omega 2023, 8, 40878−40889

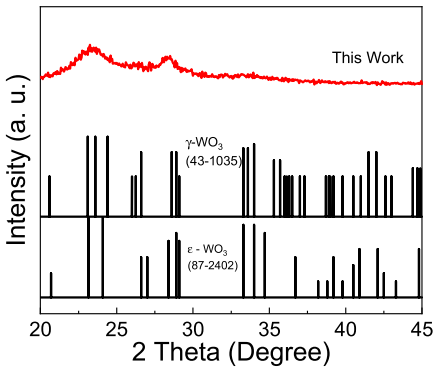

Figure 2. XRD pattern of the tungsten trioxide film prepared in this work.

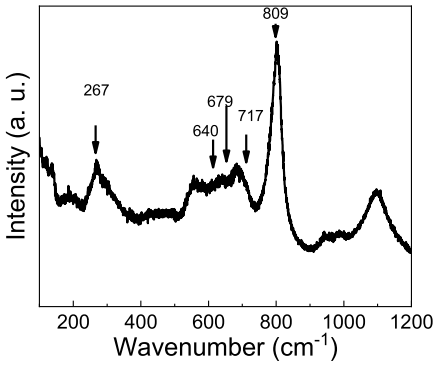

Figure 3. Raman spectrum of the WO_3 film prepared in this work.

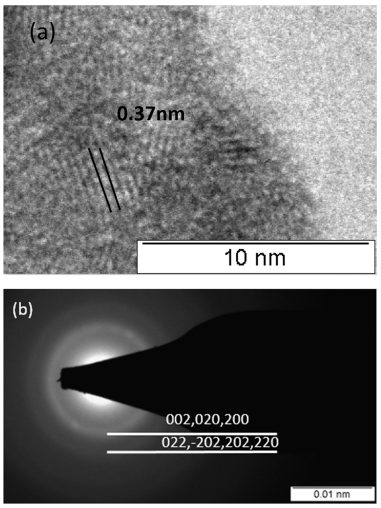

Figure 4. (a) TEM images and (b) selected electron area diffraction (SEAD) pattern obtained from WO_3 films deposited in this work.

719, and 837 cm^{-1}, and W═O stretching at 971 cm^{-1}.[57,58] Due to highly disordered sol−gel films in local bonding, broadening these features. The nanocrystalline tungsten oxide films obtained by USD and sol−gel chemistry demonstrated a single broadband in this region.

Figure 7a indicates the nitrogen physisorption isotherms and Figure 7b shows the pore size distributions and specific surface area of WO_3. The shapes of the isotherms plot of WO_3 obtained in this work correspond to type IV of the BET classification, characteristic of mesoporous materials.[59−61] The

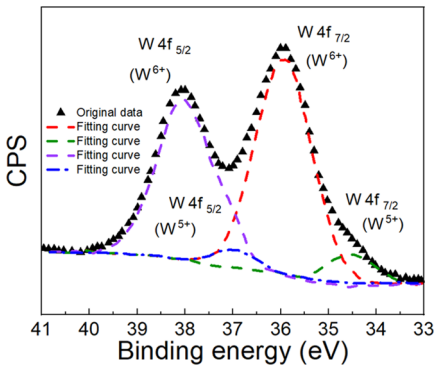

Figure 5. XPS spectra of the WO_3 thin films.

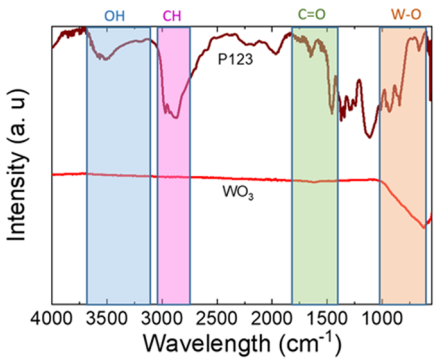

Figure 6. FTIR spectra of P123 and WO_3 films after annealing.

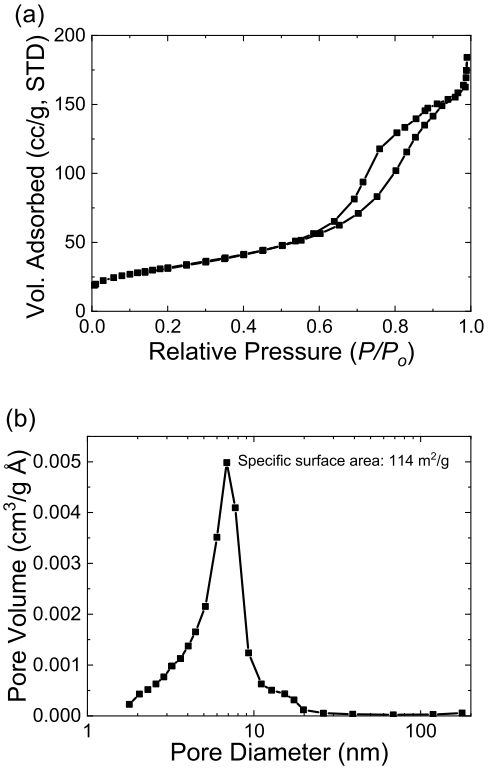

Figure 7. (a) Nitrogen physisorption isotherms obtained from mesoporous WO_3 produced in this work and (b) pore size distributions and specific surface area obtained from this work.

pore size is about 4−10 nm, and the specific surface area is 114 m^2/g.

https://doi.org/10.1021/acsomega.3c05677
ACS Omega 2023, 8, 40878−40889

3.3. Electrochemical Measurement of Mesoporous Tungsten Oxide Thin Film. In order to understand the capacitance of the deposited WO_3 film, different numbers of coats of WO_3 spraying were prepared on FTO glass, and 1 M lithium perchlorate dissolved in propylene carbonate was used as an electrolyte. Platinum electrodes were used as auxiliary electrodes, silver/silver chloride electrodes were used as reference electrodes, and constant current was applied for charging and discharging at room temperature. The difference in weight between the blank FTO glass before and after spraying was measured through an electronic balance. Then, the weight of WO_3 that is sprayed on the surface of FTO glass can be obtained. In this experiment, under the current density of 0.5 A/g, the potential range is 0 to −1.5 V. Figure 8 shows the specific capacitance measured by galvanostatic charge−discharge (GCD) under different spray coats.

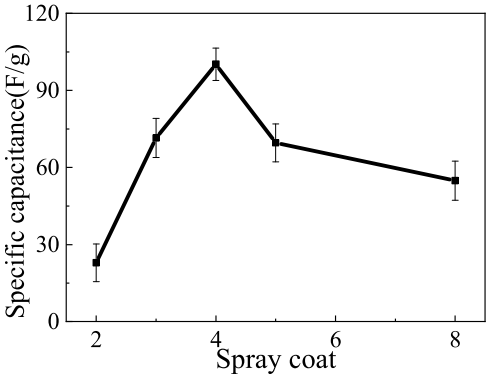

Figure 8. Relationship between specific capacitance and spray coats.

According to the specific capacitance calculation equation

$$C = \frac{It}{m\Delta V} \tag{1}$$

The value of I (current density) here is fixed at 0.5 A/g, C is the specific capacitance (F/g), t is the time (second) of charge and discharge, ΔV is the potential range (0 to −1.5 V), and m is the weight (g) of the active material. The calculated average values of specific capacitance for two, three, four, five, and eight coats are 22.86, 71.47, 100.24, 69.59, and 54.85 F/g, respectively. The specific capacitance increases with the increase of spray coats from two to four due to the increase of the active material thickness. However, the specific capacitance decreases after four coats as it is too thick, and the ion adsorption/desorption becomes difficult for the full depth of the material. Five and eight coats are chosen after four coats as thick samples.

Table 1 shows the electrochemical properties of WO_3 from different studies. It can be seen from previous literature that the specific capacitance of mesoporous WO_3 prepared by USD is better than the films prepared by other methods. This is because of the higher specific surface (114 m^2/g) area of WO_3 films were synthesized using sol−gel chemistry and USD. Higher surface area indicating more lithium ions insertion and extraction compared with the materials made in the form of bulk with low surface area using casting and calcination (36 m^2/g)[66] or hydrothermal (32.2 m^2/g).[67]

Figure 9 is the cyclic voltammogram (scan rate 10−100 mV/s) of three, four, and five spray coats with the potential range of 0 to −1.5 V, respectively. The specific capacitance of three, four, and five spray-coated mesoporous tungsten oxide electrodes is calculated according to eq 2, where v is the scan rate (V/s).

$$C = \int \frac{Idv}{2mv\Delta V} \tag{2}$$

The calculated specific capacitance value is listed in Table 2. The closed curve shown in the figure is mainly the storage behavior of the pseudocapacitance. The pseudocapacitance behavior of WO_3 is due to ion adsorption/desorption, accompanied by the relationship of reversible redox reaction between W^{6+} and W^{5+}, and its chemical reaction can be deduced as follows.

$$WO_3 + xM + +xe^- \leftrightarrow M_xWO_3 \tag{3}$$

The specific capacitance of four spray coats is higher than those of three and five coats, which is due to five coats being too thick and bad for ion adsorption/desorption on the material. It has an insufficient amount of active material for three coats. The larger specific capacitance of three coats than that of five coats indicates that thickness is a more important impede factor for capacitance.

The samples of mesoporous WO_3 sprayed three, four, and five coats were subjected to constant current charge and discharge at room temperature with three different current densities of 0.5, 1, and 2 A/g, respectively. The specific capacitance calculation is according to eq 1. Figure 10 shows the GCD curves of mesoporous tungsten oxide in the potential range of 0 to −1.5 V for three different spray coats. The specific capacitance of five spray coats is lower than that of three coats, and this is due to the large thickness of five coats

Table 1. Capacitance of Tungsten Oxide Prepared by Different Methods

material	method	the range of potential (V)	scan rate (mV/s)	electrolyte	CV specific capacitance (F/g)	current density	GCD specific capacitance (F/g)	refs
WO_3	sol−gel and USD	−1.5−0	10	1 M $LiClO_4$/PC	81.04	0.5 A/g	100.24	this work
	electrochemical deposition	−0.7−0.5	5	1 M H_2SO_4	49.3	1	42.6	43
	sol−gel	−0.7−1	20	1 M $LiClO_4$/PC	78.5			56
	sol−gel	−0.7−1		1 M $LiClO_4$/PC		2	95	62
	hydrothermal	−0.8−0.8	5	1 M Na_2SO_4	77	1	80	63
	solvothermal	−1−0.5	5	0.5 M Na_2SO_4	82	1	37	64
	ultrasonication assisted coprecipitation	−1−1	30	0.1 M KCl	0.058			65

https://doi.org/10.1021/acsomega.3c05677
ACS Omega 2023, 8, 40878−40889

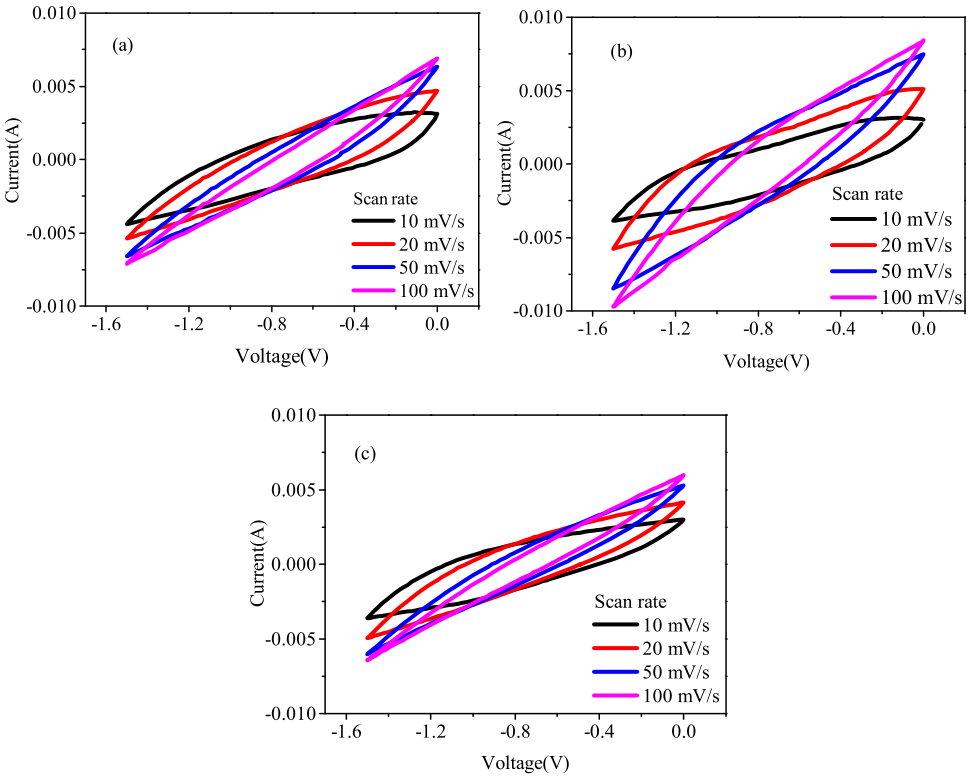

Figure 9. Cyclic voltammogram of different spray coats with different scan rates: (a) three, (b) four, and (c) five coats.

Table 2. Specific Capacitance of Three, Four, and Five Spray Coats with Different Scan Rates

scan rate (mV/s)	specific capacitance (F/g) three coats	four coats	five coats
10	73.94	94.21	33.94
20	32.97	64.41	17.10
50	10.07	25.75	4.90
100	3.53	9.93	1.69

blocking the adsorption/desorption of the material. The specific capacitance of three coats is higher than that of five coats, which also indicates that thickness is a more important factor for capacitance.

Figure 11 shows the GCD curves of three, four, and five spray coats at a current density of 0.5 A/g, and the capacitance values are 85.42, 109.15, and 66.89 F/g, respectively. Figure 12 shows the relationship between current density and specific capacitance. The specific capacitance values were calculated by eq 1. It can be seen that the specific capacitance of mesoporous WO_3 sprayed four coats is better than that of other spray coats. The low specific capacitance of five spray coats than that of three coats can be because the thick film is not good for ion adsorption/desorption on the material. For the same spray coats, the specific capacitance follows the order 2 A/g < 1 A/g < 0.5 A/g. At higher current densities, intercalation of lithium ions into the inner active sites of material becomes more difficult, and the specific capacitance is reduced.

Figure 13 is the Ragone plot of the power density and energy density of the mesoporous WO_3 electrode with four spray coats. The energy density is calculated by eq 4 and the power density is calculated by eq 5. E is the energy density (Wh/kg) and P is the power density (W/kg).

$$E = 0.5 \times C(\Delta V)^2 \quad (4)$$

$$P = E/\Delta t \quad (5)$$

The calculated energy density at 0.5 A/g is 32.28 Wh/kg with a power density of 219.53 W/kg, 1 A/g of 18.52 Wh/kg with a power density of 415.03 W/kg, and 2 A/g of 8.01 Wh/kg with a power density of 659.15 W/kg.

Figure 14 shows a graph of the relationship between the number of spray coats and the film thickness. It can be seen that it shows a linear relationship, indicating that ultrasonic spraying can accurately control the film thickness through the number of spray coats. The plot of the relationship between film thickness and specific capacitance is shown in Figure 15, and it can be found that the number of spray coats affects the thickness of the film and has a greater impact on its capacitance. It is pointed out from the literature[68] that if the thickness of the electrode layer is thinner, because there are fewer active materials on the electrode, it cannot provide higher capacitance. More active material contained in a relatively thick electrode layer can provide a higher capacitance. If the thickness of the electrode is too large, the capacitance is reduced. This is because the increase in the electrode thickness will cause the transfer of electrolyte ions into and out of the active layer to be even more difficult. The depth of the electrolyte ions entering the active layer becomes shallow; therefore, there is an optimized electrode layer thickness. Figure 16 is the SEM cross-sectional view of the mesoporous WO_3 sprayed four coats, and the film thickness of mesoporous WO_3 is about 1.36 μm, which is the optimized film thickness for specific capacitance in this study.

Figure 17 shows the stability of the mesoporous WO_3 electrode sprayed four coats. A 1 M lithium perchlorate in propylene carbonate was used as the electrolyte, and constant current was applied to the sample at 0.3 A/g in the potential

https://doi.org/10.1021/acsomega.3c05677
ACS Omega 2023, 8, 40878−40889

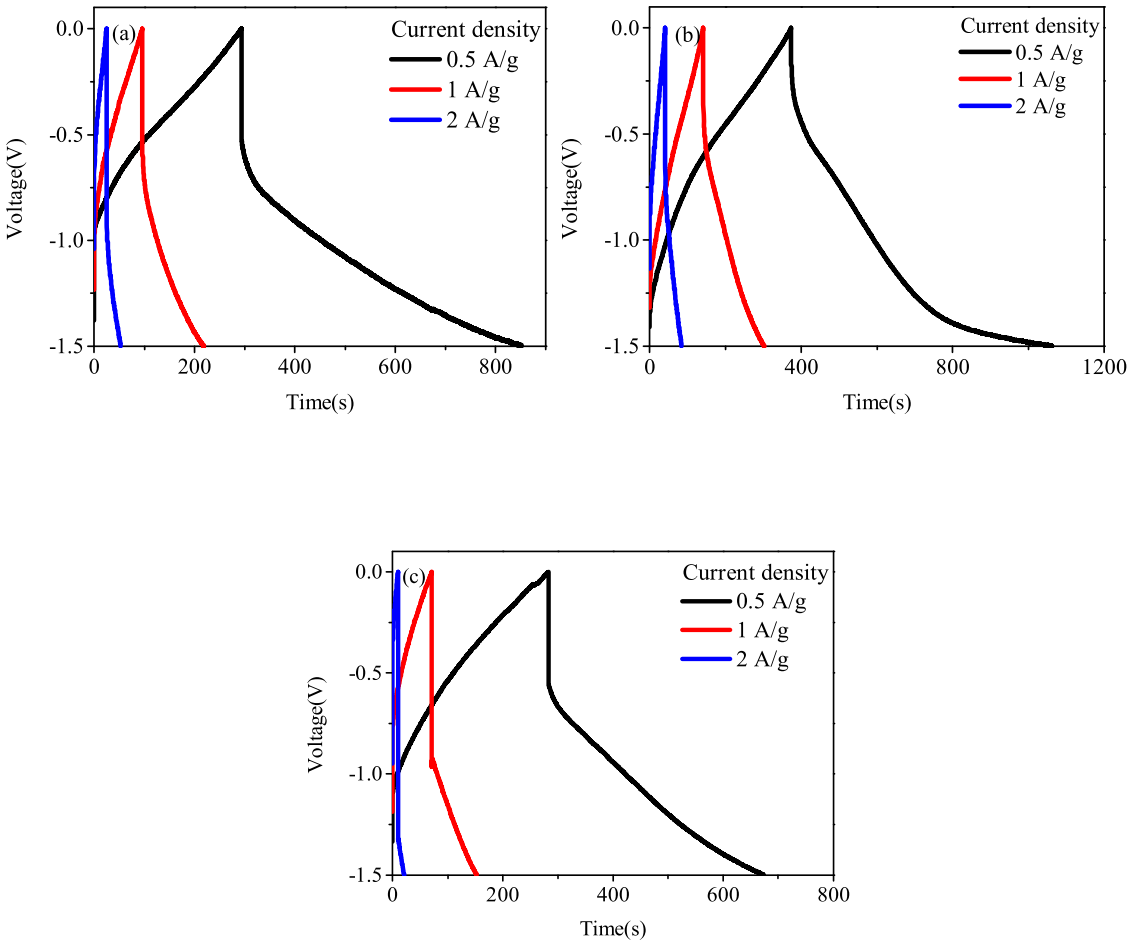

Figure 10. GCD plots at different current densities under different spray coats: (a) three, (b) four, and (c) five coats.

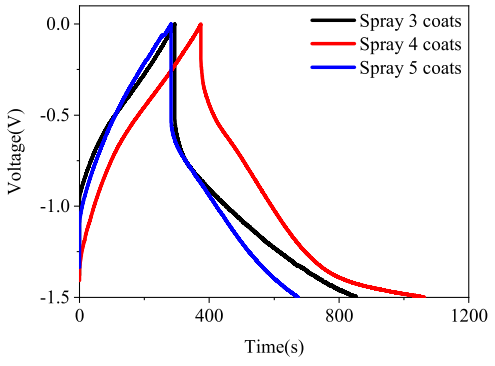

Figure 11. GCD curves of mesoporous WO_3 with different spray coats at a constant current density of 0.5 A/g.

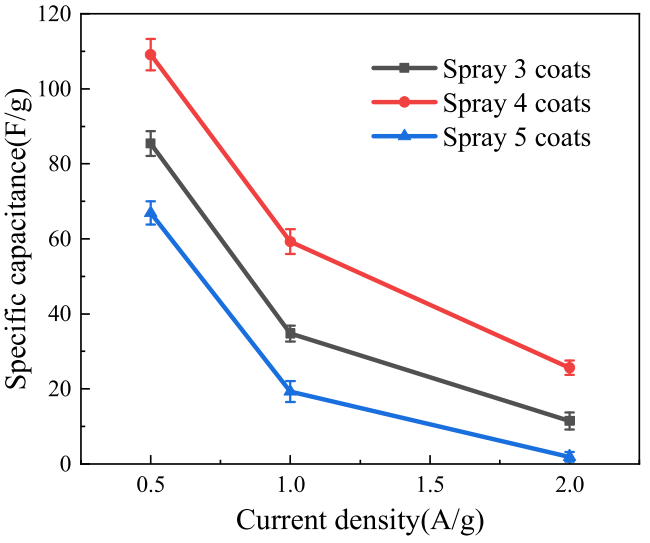

Figure 12. Relationship between current density and specific capacitance under different spray coats.

range of 0 to −0.9 V. It can be found that the capacitance drops rapidly in the first 100 cycles, which can be attributed to the irreversible chemical reaction in the process of charging and discharging. The chemical reaction leads to the disappearance of the surface oxidation function, thus losing the pseudocapacitive properties of the surface.[69] As the number of cycles progresses, the wettability of the electrode material becomes better or the active material that has not been activated is gradually activated, and the capacitance increases slightly. From Figure 17, it can be found that the ultrasonic sprayed mesoporous WO_3 has good stability. After 4000 cycles of constant current charging and discharging, it can be seen that the specific capacitance value maintenance rate is still 84% of the initial cycle. The adsorption and desorption of lithium ions cause the material to detach from the films in a liquid solution. Actually, the durability will be greatly improved if the film can be encapsulated by a solid-state electrolyte during device fabrication. The durability of WO_3

https://doi.org/10.1021/acsomega.3c05677
ACS Omega 2023, 8, 40878−40889

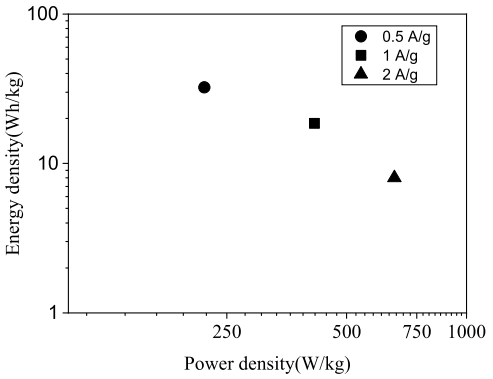

Figure 13. Ragone plot of the energy density and power density of mesoporous tungsten oxide under different current densities.

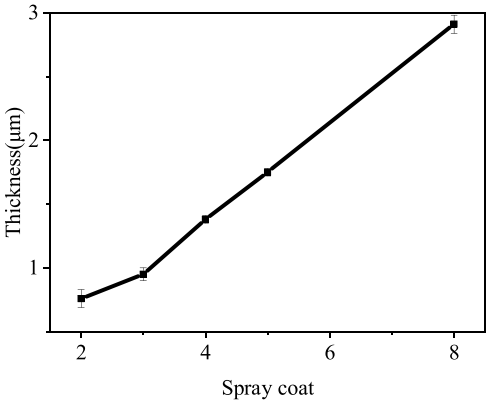

Figure 14. Relationship between the number of spray coats and the film thickness.

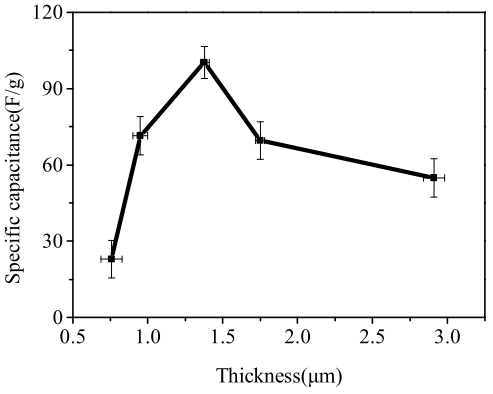

Figure 15. Relationship between specific capacitance and the film thickness.

film in this work is much better than that of previous reports (37.5% specific capacitance deterioration after 200 cycles)[41] due to the stable characteristic of the nancrystalline WO_3 made from the combination of template-assisted sol−gel chemistry and USD technique.

In order to understand the relationship between the spray coats and the resistance of the mesoporous tungsten oxide electrode, electrochemical impedance spectroscopy (EIS) was used to perform the AC impedance/constant potentiometer (SP-150) measurements with a frequency range of 40 kHz to 100 mHz using the 1 M lithium perchlorate in propylene carbonate as the electrolyte at room temperature. Figure 18 shows the AC impedance diagram of three, four, and five spray

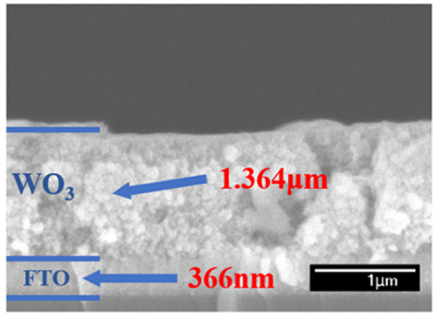

Figure 16. SEM cross-sectional view of the mesoporous WO_3 sprayed in four coats.

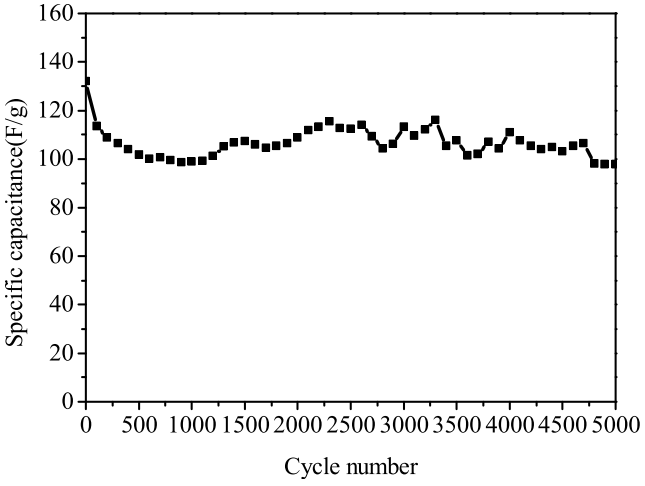

Figure 17. Specific capacitance stability of the mesoporous tungsten oxide electrode sprayed four coats under 5000 cycles at a constant current density of 0.3 A/g.

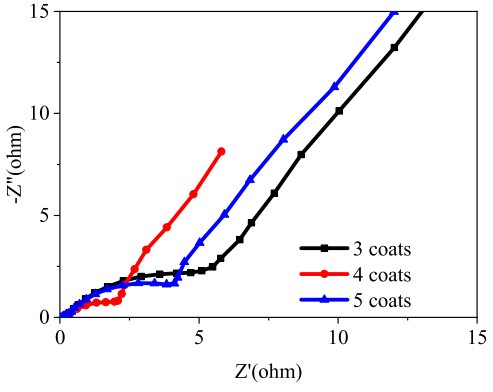

Figure 18. Overlay of Nyquist diagrams with different spray coats.

coats. The figure exhibits a straight line in the low-frequency area and part of the semicircle in the high-frequency area. The diameter of the semicircle corresponds to the charge transfer resistance (R_{ct}).

The enlarged high-frequency area is shown in Figure 19. In the high-frequency area, the R_{ct} of the mesoporous WO_3 electrode is 4.703, 2.081, and 3.833 Ω for spray three, four, and five coats, respectively. The R_{ct} value of four spray coats is the smallest, about 2.25 times smaller than that of three spray coats and about 1.84 times smaller than five spray coats. Through this experiment, it can be obtained that the number of spray coats affects the thickness of the film and has a greater

https://doi.org/10.1021/acsomega.3c05677
ACS Omega 2023, 8, 40878−40889

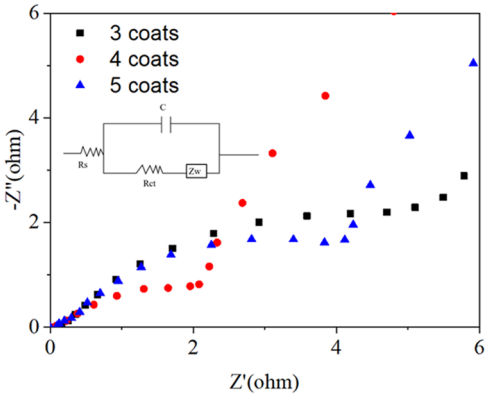

Figure 19. Enlarged high-frequency area of Nyquist diagrams with different spray coats.

impact on its capacitance. When the film has a too low number of spray coats, because of the small amount of active material and high impedance, the measured capacitance is small. The mesoporous WO_3 with more spray coats and larger film thickness, although its impedance is relatively low, its small capacitance is speculated that too thick a film will be unfavorable for the entry and exit of lithium ions in the electrolyte.

The R_{ct} of four spray coats shows a large value of 2.081 Ω at 0.75 V, indicating that the charge exchange and compensation at the material−solution interface at this potential are more difficult. This R_{ct} (2.081 Ω) is based on the low conductivity of WO_3 at such high positive potentials.[41]

From previous reports, it can be found that the hydrothermal method is currently the mainstream method to prepare nanoscale tungsten oxide. Compared with the high-temperature and high-pressure conditions and special processing equipment required by the hydrothermal method,[23,24,26,66,69−83] the preparation of WO_3 by the sol−gel method and USD in this experiment has many advantages. For example, it can be synthesized at a low temperature, requires less equipment, can be freely customized, the ratio can be adjusted according to the materials, product uniformity is easy to achieve, and precise control of the film structure is easy, such as porosity, specific surface area, etc. In this study, the common lithium salt is used in the electrolyte. The electrolyte used in the previous literature[23,24,26,66,69,73−82] is usually a high-concentration strong acid (such as H_2SO_4) because the dissociated hydrogen ions are smaller than lithium ions. It is relatively easy in terms of capacitance; therefore, the capacitance is usually much higher than that of lithium ions. From the literature, the specific capacitance was in the range of 545−797 F/g when WO_3 materials were obtained from the hydrothermal method[78,84,85] and 465−588 F/g from the solvothermal method.[74,75] High-concentration strong acids are highly dangerous. Once the liquid leaks, it will cause harm to the human body and organisms that come into contact with it and strong acids will pollute the environment. The recycling of a strong acid is not easy. Lithium salts are quite safe and environmentally friendly, which is suitable for use in a wearable device.

4. CONCLUSIONS

In this study, ultrasonic spray deposition combined with the sol−gel method was used to manufacture mesoporous WO_3 electrodes. By adjusting the number of spray coats, the thickness of the mesoporous WO_3 film can be controlled and the capacitance can be optimized. It has a specific capacitance of 94.21 F/g at a scan rate of 10 mv/s, and a specific capacitance of 109.15 F/g at a current density of 0.5 A/g. The film thickness affects impedance and specific capacitance. After 5000 cycles of charging and discharging in the long-term cycling test, its performance indicates its good capacitance stability. The superior energy storage capacity of mesoporous WO_3 films and promising USD technique exhibit competitive advantages in the market.

AUTHOR INFORMATION

Corresponding Author

Chi-Ping Li − *Department of Chemical Engineering, National United Unversity, 360302 Maioli, Taiwan;* orcid.org/0000-0003-4978-9957; Email: chipingli@nuu.edu.tw

Author

Gui Yang Lai − *Department of Materials Science and Engineering, National United University, 360302 Maioli, Taiwan*

Complete contact information is available at: https://pubs.acs.org/10.1021/acsomega.3c05677

Author Contributions

C.-P.L. conceptualized the study, developed the methodology, and performed the validation. methodology. C.-P.L. and G.Y.L. performed the formal analysis. C.-P.L. and G.Y.L. curated the data. C.-P.L. wrote the original draft and reviewed and edited the manuscript. All authors have read and agreed to the published version of the manuscript.

Notes

The authors declare no competing financial interest.

ACKNOWLEDGMENTS

The authors thank the funding from the National Science and Technology Council of Taiwan (grant number NTSC 111-2622-E-239-008).

REFERENCES

(1) Du, X.; Chengyang, W.; Mingming, C.; Yang, J.; Jin, W. Electrochemical Performances of Nanoparticle Fe3O 4/Activated Carbon Supercapacitor Using KOH Electrolyte Solution. *J. Phys. Chem. C* **2009**, *113* (6), 2643−2646.

(2) Qu, Q. T.; Shi, Y.; Tian, S.; Chen, Y. H.; Wu, Y. P.; Holze, R. A New Cheap Asymmetric Aqueous Supercapacitor: Activated Carbon//NaMnO2. *J. Power Sources* **2009**, *194* (2), 1222−1225.

(3) Wang, G.; Wang, H.; Lu, X.; Ling, Y.; Yu, M.; Zhai, T.; Tong, Y.; Li, Y. Solid-State Supercapacitor Based on Activated Carbon Cloths Exhibits Excellent Rate Capability. *Adv. Mater.* **2014**, *26* (17), 2676−2682.

(4) Li, B.; Dai, F.; Xiao, Q.; Yang, L.; Shen, J.; Zhang, C.; Cai, M. Nitrogen-Doped Activated Carbon for a High Energy Hybrid Supercapacitor. *Energy Environ. Sci.* **2016**, *9* (1), 102−106.

(5) Shiraishi, S.; Kurihara, H.; Okabe, K.; Hulicova, D.; Oya, A. Electric Double Layer Capacitance of Highly Pure Single-Walled Carbon Nanotubes (HiPcoe Buckytubese) in Propylene Carbonate Electrolytes. *Electrochem. Commun. 4*, 593 598. DOI: 10.1016/s1388-2481(02)00382-x.

(6) Li, Q. Y.; Li, Z. S.; Lin, L.; Wang, X. Y.; Wang, Y. F.; Zhang, C. H.; Wang, H. Q. Facile Synthesis of Activated Carbon/Carbon Nanotubes Compound for Supercapacitor Application. *Chem. Eng. J.* **2010**, *156* (2), 500−504.

https://doi.org/10.1021/acsomega.3c05677
ACS Omega 2023, 8, 40878−40889

(7) Wang, Y.; Shi, Z.; Huang, Y.; Ma, Y.; Wang, C.; Chen, M.; Chen, Y. Supercapacitor Devices Based on Graphene Materials. *J. Phys. Chem. C* **2009**, *113* (30), 13103−13107.
(8) Kim, T.; Jung, G.; Yoo, S.; Suh, K. S.; Ruoff, R. S. Activated Graphene-Based Carbons as Supercapacitor Electrodes with Macro- and Mesopores. *ACS Nano* **2013**, *7* (8), 6899−6905.
(9) Portet, C.; Yushin, G.; Gogotsi, Y. Electrochemical Performance of Carbon Onions, Nanodiamonds, Carbon Black and Multiwalled Nanotubes in Electrical Double Layer Capacitors. *Carbon* **2007**, *45* (13), 2511−2518.
(10) Pech, D.; Brunet, M.; Durou, H.; Huang, P.; Mochalin, V.; Gogotsi, Y.; Taberna, P. L.; Simon, P. Ultrahigh-Power Micrometre-Sized Supercapacitors Based on Onion-like Carbon. *Nat. Nanotechnol.* **2010**, *5* (9), 651−654.
(11) Saliger, R.; Fischer, U.; Herta, C.; Fricke, J. High Surface Area Carbon Aerogels for Supercapacitors. *J. Non-Cryst. Solids* **1998**, *225*, 81−85, DOI: 10.1016/s0022-3093(98)00104-5.
(12) Lin, C.; Ritter, J. A.; Popov, B. N. Correlation of Double-Layer Capacitance with the Pore Structure of Sol-Gel Derived Carbon Xerogels. *J. Electrochem. Soc.* **1999**, *146* (10), 3639−3643.
(13) Fuertes, A. B.; Pico, F.; Rojo, J. M. Influence of Pore Structure on Electric Double-Layer Capacitance of Template Mesoporous Carbons. *J. Power Sources* **2004**, *133* (2), 329−336.
(14) Huczko, A. Template-Based Synthesis of Nanomaterials. *Appl. Phys. A: Mater. Sci. Process.* **2000**, *70*, 365−376.
(15) Lust, E.; Nurk, G.; Jänes, A.; Arulepp, M.; Nigu, P.; Möller, P.; Kallip, S.; Sammelselg, V. Electrochemical Properties of Nanoporous Carbon Electrodes in Various Nonaqueous Electrolytes. *J. Solid State Electrochem.* **2003**, *7*, 91−105, DOI: 10.1007/s10008-002-0316-1.
(16) Chmiola, J.; Yushin, G.; Dash, R. K.; Hoffman, E. N.; Fischer, J. E.; Barsoum, M. W.; Gogotsi, Y. Double-Layer Capacitance of Carbide Derived Carbons in Sulfuric Acid. *Electrochem. Solid-State Lett.* **2005**, *8* (7), No. A357, DOI: 10.1149/1.1921134.
(17) Chmiola, J.; Yushin, G.; Dash, R.; Gogotsi, Y. Effect of Pore Size and Surface Area of Carbide Derived Carbons on Specific Capacitance. *J. Power Sources* **2006**, *158* (1), 765−772.
(18) Wang, G.; Zhang, L.; Zhang, J. A Review of Electrode Materials for Electrochemical Supercapacitors. *Chem. Soc. Rev.* **2012**, *41* (2), 797−828.
(19) Liu, X.; Pickup, P. G. Ru Oxide Supercapacitors with High Loadings and High Power and Energy Densities. *J. Power Sources* **2008**, *176* (1), 410−416.
(20) Xia, H.; Li, B.; Lu, L. 1.8 v Symmetric Supercapacitors Developed Using Nanocrystalline Ru Films as Electrodes. *RSC Adv.* **2014**, *4* (22), 11111−11114.
(21) Gujar, T. P.; Shinde, V. R.; Lokhande, C. D.; Kim, W. Y.; Jung, K. D.; Joo, O. S. Spray Deposited Amorphous RuO2 for an Effective Use in Electrochemical Supercapacitor. *Electrochem. Commun.* **2007**, *9* (3), 504−510.
(22) Subramanian, V.; Hall, S. C.; Smith, P. H.; Rambabu, B. Mesoporous Anhydrous RuO2 as a Supercapacitor Electrode Material. *Solid State Ionics* **2004**, *175*, 511−515.
(23) Yin, Z.; Bu, Y.; Ren, J.; Chen, S.; Zhao, D.; Zou, Y.; Shen, S.; Yang, D. Triggering Superior Sodium Ion Adsorption on (2 0 0) Facet of Mesoporous WO3 Nanosheet Arrays for Enhanced Supercapacitance. *Chem. Eng. J.* **2018**, *345*, 165−173.
(24) Wu, X.; Yao, S. Flexible Electrode Materials Based on WO3 Nanotube Bundles for High Performance Energy Storage Devices. *Nano Energy* **2017**, *42*, 143−150.
(25) Kadi, M. W.; Mohamed, R. M.; Ismail, A. A.; Bahnemann, D. W. Soft and Hard Templates Assisted Synthesis Mesoporous CuO/g-C3N4 Heterostructures for Highly Enhanced and Accelerated Hg(II) Photoreduction under Visible Light. *J. Colloid Interface Sci.* **2020**, *580*, 223−233.
(26) Han, Z.; Ren, J.; Zhou, J.; Zhang, S.; Zhang, Z.; Yang, L.; Yin, C. Multilayer Porous Pd-WO3 Composite Thin Films Prepared by Sol-Gel Process for Hydrogen Sensing. *Int. J. Hydrogen Energy* **2020**, *45* (11), 7223−7233.
(27) Sial, Q. A.; Javed, M. S.; Lee, Y. J.; Duy, L. T.; Seo, H. Flexible and Transparent Graphene-Based Supercapacitors Decorated with Nanohybrid of Tungsten Oxide Nanoflakes and Nitrogen-Doped-Graphene Quantum Dots. *Ceram. Int.* **2020**, *46* (14), 23145−23154.
(28) Guo, Q.; Zhao, X.; Li, Z.; Wang, D.; Nie, G. A Novel Solid-State Electrochromic Supercapacitor with High Energy Storage Capacity and Cycle Stability Based on Poly(5-Formylindole)/WO3 Honeycombed Porous Nanocomposites. *Chem. Eng. J.* **2020**, *384*, No. 123370.
(29) Parashar, M.; Shukla, V. K.; Singh, R. Metal Oxides Nanoparticles via Sol−Gel Method: A Review on Synthesis, Characterization and Applications. *J. Mater. Sci.: Mater. Electron.* **2020**, *31* (5), 3729−3749.
(30) Guan, X. H.; Zhang, Z. W.; Yang, L.; Wang, G. S. One-Pot Hydrothermal Synthesis of Hexagonal WO3 Nanorods/Graphene Composites as High-Performance Electrodes for Supercapacitors. *ChemPlusChem* **2017**, *82* (9), 1174−1181.
(31) Yao, S.; Zheng, X.; Zhang, X.; Xiao, H.; Qu, F.; Wu, X. Facile Synthesis of Flexible WO3 Nanofibers as Supercapacitor Electrodes. *Mater. Lett.* **2017**, *186*, 94−97.
(32) Tenent, R. C.; Gillaspie, D. T.; Miedaner, A.; Parilla, P. A.; Curtis, C. J.; Dillon, A. C. Fast-Switching Electrochromic Li[Sup +]-Doped NiO Films by Ultrasonic Spray Deposition. *J. Electrochem. Soc.* **2010**, *157* (3), No. H318.
(33) Li, C. P.; Lin, F.; Richards, R. M.; Engtrakul, C.; Dillon, A. C.; Tenent, R. C.; Wolden, C. A. Ultrasonic Spray Deposition of High Performance WO 3 Films Using Template-Assisted Sol-Gel Chemistry. *Electrochem. Commun.* **2012**, *25* (1), 62−65.
(34) Au, B. W. C.; Chan, K. Y.; Pang, W. L.; Lee, C. L.; Mustafa, A. H. Tungsten Oxide (Wo3) Films Prepared by Sol-Gel Spin-Coating Technique. *Solid State Phenom.* **2018**, *280*, 71−75, DOI: 10.4028/www.scientific.net/ssp.280.71.
(35) Ozkan, E.; Lee, S. H.; Liu, P.; Tracy, C. E.; Tepehan, F. Z.; Pitts, J. R.; Deb, S. K. Electrochromic and Optical Properties of Mesoporous Tungsten Oxide Films. *Solid State Ionics* **2002**, *149* (1−2), 139−146.
(36) Hilliard, S.; Baldinozzi, G.; Friedrich, D.; Kressman, S.; Strub, H.; Artero, V.; Laberty-Robert, C. Mesoporous Thin Film WO3 Photoanode for Photoelectrochemical Water Splitting: A Sol-Gel Dip Coating Approach. *Sustainable Energy Fuels* **2017**, *1* (1), 145−153.
(37) Wang, W. Q.; Yao, Z. J.; Wang, X. L.; Xia, X. H.; Gu, C. D.; Tu, J. P. Niobium Doped Tungsten Oxide Mesoporous Film with Enhanced Electrochromic and Electrochemical Energy Storage Properties. *J. Colloid Interface Sci.* **2019**, *535*, 300−307.
(38) Vernardou, D.; Drosos, H.; Spanakis, E.; Koudoumas, E.; Katsarakis, N.; Pemble, M. E. Electrochemical Properties of Amorphous WO 3 Coatings Grown on Polycarbonate by Aerosol-Assisted CVD. *Electrochim. Acta* **2012**, *65*, 185−189.
(39) Shi, Y.; Sun, M.; Chen, W.; Zhang, Y.; Shu, X.; Qin, Y.; Zhang, X.; Shen, H.; Wu, Y. Rational Construction of Porous Amorphous WO3 Nanostructures with High Electrochromic Energy Storage Performance: Effect of Temperature. *J. Non-Cryst. Solids* **2020**, *549*, No. 120337.
(40) Gui, Y.; Blackwood, D. J. Capacitive Desalination of WO3/Carbon Cloth Supercapacitor and Morphology Analysis. *Water Pract. Technol.* **2018**, *13* (2), 410−413.
(41) Zou, B. X.; Liang, Y.; Liu, X. X.; Diamond, D.; Lau, K. T. Electrodeposition and Pseudocapacitive Properties of Tungsten Oxide/Polyaniline Composite. *J. Power Sources* **2011**, *196* (10), 4842−4848.
(42) Xie, S.; Bi, Z.; Chen, Y.; He, X.; Guo, X.; Gao, X.; Li, X. Electrodeposited Mo-Doped WO 3 Film with Large Optical Modulation and High Areal Capacitance toward Electrochromic Energy-Storage Applications. *Appl. Surf. Sci.* **2018**, *459*, 774−781.
(43) Firat, Y. E. Pseudocapacitive Energy Storage Properties of RGO-WO3 Electrode Synthesized by Electrodeposition. *Mater. Sci. Semicond. Process.* **2021**, *133*, No. 105938.
(44) Marcu, M.; Preda, L.; Vizireanu, S.; Bita, B.; Mihai, M. A.; Spataru, T.; Acsente, T.; Dinescu, G.; Spataru, N. Enhancement of the

https://doi.org/10.1021/acsomega.3c05677
ACS Omega 2023, 8, 40878−40889

Capacitive Features of WO3 Supported on Pristine and Functionalized Graphite by Appropriate Adjustment of the Electrodeposition Regime. *Mater. Sci. Eng. B* **2022**, *277*, No. 115585.
(45) Jin, L. N.; Liu, P.; Jin, C.; Zhang, J. N.; Bian, S. W. Porous WO3/Graphene/Polyester Textile Electrode Materials with Enhanced Electrochemical Performance for Flexible Solid-State Supercapacitors. *J. Colloid Interface Sci.* **2018**, *510*, 1−11.
(46) Li, C. P.; Engtrakul, C.; Tenent, R. C.; Wolden, C. A. Scalable Synthesis of Improved Nanocrystalline, Mesoporous Tungsten Oxide Films with Exceptional Electrochromic Performance. *Sol. Energy Mater. Sol. Cells* **2015**, *132*, 6−14.
(47) Mai, Y.; Zhang, F.; Feng, X. Polymer-Directed Synthesis of Metal Oxide-Containing Nanomaterials for Electrochemical Energy Storage. *Nanoscale* **2014**, *6* (1), 106−121.
(48) Li, C. P.; Wolden, C. A.; Dillon, A. C.; Tenent, R. C. Electrochromic Films Produced by Ultrasonic Spray Deposition of Tungsten Oxide Nanoparticles. *Sol. Energy Mater. Sol. Cells* **2012**, *99*, 50−55.
(49) Lee, S. H.; Deshpande, R.; Parilla, P. A.; Jones, K. M.; To, B.; Mahan, A. H.; Dillon, A. C. Crystalline WO3 Nanoparticles for Highly Improved Electrochromic Applications. *Adv. Mater.* **2006**, *18* (6), 763−766.
(50) Gupta, S. P.; Nishad, H. H.; Chakane, S. D.; Gosavi, S. W.; Late, D. J.; Walke, P. S. Phase Transformation in Tungsten Oxide Nanoplates as a Function of Post-Annealing Temperature and Its Electrochemical Influence on Energy Storage. *Nanoscale Adv.* **2020**, *2* (10), 4689−4701.
(51) Can, F.; Courtois, X.; Duprez, D. Tungsten-based Catalysts for Environmental Applications. *Catalysts* **2021**, *11* (6), No. 703.
(52) Nunes, S. E.; Matte, L. C.; da Cunha, C. R. Producing Oxygen-Rich WO3 Thin Films by Post-Deposition Thermal Annealing. *Mater. Res. Express* **2019**, *6* (9), No. 095905.
(53) Sun, S.; Wu, J.; Watanabe, M.; Akbay, T.; Ishihara, T. Single-Electron-Trapped Oxygen Vacancy on Ultrathin WO3·0.33H2O {100} Facets Suppressing Backward Reaction for Promoted H2 Evolution in Pure Water Splitting. *J. Phys. Chem. Lett.* **2019**, *10* (11), 2998−3005.
(54) Cong, S.; Tian, Y.; Li, Q.; Zhao, Z.; Geng, F. Single-Crystalline Tungsten Oxide Quantum Dots for Fast Pseudocapacitor and Electrochromic Applications. *Adv. Mater.* **2014**, *26* (25), 4260−4267.
(55) Hu, A.; Jiang, Z.; Kuai, C.; McGuigan, S.; Nordlund, D.; Liu, Y.; Lin, F. Uncovering Phase Transformation, Morphological Evolution, and Nanoscale Color Heterogeneity in Tungsten Oxide Electrochromic Materials. *J. Mater. Chem. A* **2020**, *8* (38), 20000−20010.
(56) Koo, B. R.; Jo, M. H.; Kim, K. H.; Ahn, H. J. Amorphous-Quantized WO3·H2O Films as Novel Flexible Electrode for Advanced Electrochromic Energy Storage Devices. *Chem. Eng. J.* **2021**, *424*, No. 130383.
(57) Polleux, J.; Antonietti, M.; Niederberger, M. Ligand and Solvent Effects in the Nonaqueous Synthesis of Highly Ordered Anisotropic Tungsten Oxide Nanostructures. *J. Mater. Chem.* **2006**, *16* (40), 3969−3975.
(58) Deepa, M.; Joshi, A. G.; Srivastava, A. K.; Shivaprasad, S. M.; Agnihotry, S. A. Electrochromic Nanostructured Tungsten Oxide Films by Sol-Gel: Structure and Intercalation Properties. *J. Electrochem. Soc.* **2006**, *153* (5), No. C365.
(59) Rougier, A.; Portemer, F.; Quédé, A.; El Marssi, M. Characterization of Pulsed Laser Deposited WO3 Thin Films for Electrochromic Devices. *Appl. Surf. Sci.* **1999**, *153* (1), 1−9.
(60) Leftheriotis, G.; Papaefthimiou, S.; Yianoulis, P. The Effect of Water on the Electrochromic Properties of WO3 Films Prepared by Vacuum and Chemical Methods. *Sol. Energy Mater. Sol. Cells* **2004**, *83* (1), 115−124.
(61) Yang, P.; Zhao, D.; Margolese, D. I.; Chmelka, B. F.; Stucky, G. D. Generalized Syntheses of Large-Pore Mesoporous Metal Oxides with Semicrystalline Frameworks. *Nature* **1998**, *396* (6707), 152−155.
(62) Koo, B. R.; Jo, M. H.; Kim, K. H.; Ahn, H. J. Multifunctional Electrochromic Energy Storage Devices by Chemical Cross-Linking: Impact of a WO3·H2O Nanoparticle-Embedded Chitosan Thin Film on Amorphous WO3 Films. *NPG Asia Mater.* **2020**, *12* (1), No. 10, DOI: 10.1038/s41427-019-0193-z.
(63) Haldar, P. Achieving Wide Potential Window and High Capacitance for Supercapacitors Using Different Metal Oxides (Viz.: ZrO2, WO3 and V2O5) and Their PANI/Graphene Composites with Na2SO4 Electrolyte. *Electrochim. Acta* **2021**, *381*, No. 138221.
(64) Rudra, S.; K, J.; Thamizharasan, G.; Pradhan, M.; Rani, B.; Sahu, N. K.; Nayak, A. K. Fabrication of Mn3O4-WO3 Nanoparticles Based Nanocomposites Symmetric Supercapacitor Device for Enhanced Energy Storage Performance under Neutral Electrolyte. *Electrochim. Acta* **2022**, *406*, No. 139870.
(65) Gurushantha, K.; Kottam, N.; Smrithi, S. P.; Dharmaprakash, M. S.; Keshavamurthy, K.; Meena, S.; Srinatha, N. Visible Light Active WO3/TiO2 Heterojunction Nanomaterials for Electrochemical Sensor, Capacitance and Photocatalytic Applications. *Catal. Lett.* **2023**, 1−12, DOI: 10.1007/s10562-023-04362-7.
(66) Wang, Y. H.; Wang, C. C.; Cheng, W. Y.; Lu, S. Y. Dispersing WO3 in Carbon Aerogel Makes an Outstanding Supercapacitor Electrode Material. *Carbon* **2014**, *69*, 287−293.
(67) Gupta, S. P.; Patil, V. B.; Tarwal, N. L.; Bhame, S. D.; Gosavi, S. W.; Mulla, I. S.; Late, D. J.; Suryavanshi, S. S.; Walke, P. S. Enhanced Energy Density and Stability of Self-Assembled Cauliflower of Pd Doped Monoclinic WO3 Nanostructure Supercapacitor. *Mater. Chem. Phys.* **2019**, *225*, 192−199.
(68) Tsay, K. C.; Zhang, L.; Zhang, J. Effects of Electrode Layer Composition/Thickness and Electrolyte Concentration on Both Specific Capacitance and Energy Density of Supercapacitor. *Electrochim. Acta* **2012**, *60*, 428−436.
(69) Yao, S.; Qu, F.; Wang, G.; Wu, X. Facile Hydrothermal Synthesis of WO3 Nanorods for Photocatalysts and Supercapacitors. *J. Alloys Compd.* **2017**, *724*, 695−702.
(70) Wang, R.; Lu, Y.; Zhou, L.; Han, Y.; Ye, J.; Xu, W.; Lu, X. Oxygen-Deficient Tungsten Oxide Nanorods with High Crystallinity: Promising Stable Anode for Asymmetric Supercapacitors. *Electrochim. Acta* **2018**, *283*, 639−645.
(71) Shinde, P. A.; Lokhande, A. C.; Patil, A. M.; Lokhande, C. D. Facile Synthesis of Self-Assembled WO3 Nanorods for High-Performance Electrochemical Capacitor. *J. Alloys Compd.* **2019**, *770*, 1130−1137.
(72) Shinde, P. A.; Lokhande, A. C.; Chodankar, N. R.; Patil, A. M.; Kim, J. H.; Lokhande, C. D. Temperature Dependent Surface Morphological Modifications of Hexagonal WO3 Thin Films for High Performance Supercapacitor Application. *Electrochim. Acta* **2017**, *224*, 397−404.
(73) Gao, L.; Wang, X.; Xie, Z.; Song, W.; Wang, L.; Wu, X.; Qu, F.; Chen, D.; Shen, G. High-Performance Energy-Storage Devices Based on WO3 Nanowire Arrays/Carbon Cloth Integrated Electrodes. *J. Mater. Chem. A* **2013**, *1* (24), 7167−7173.
(74) Nayak, A. K.; Das, A. K.; Pradhan, D. High Performance Solid-State Asymmetric Supercapacitor Using Green Synthesized Graphene-WO3 Nanowires Nanocomposite. *ACS Sustainable Chem. Eng.* **2017**, *5* (11), 10128−10138.
(75) Jung, J.; Kim, D. H. W 18 O 49 Nanowires Assembled on Carbon Felt for Application to Supercapacitors. *Appl. Surf. Sci.* **2018**, *433*, 750−755.
(76) Upadhyay, K. K.; Altomare, M.; Eugénio, S.; Schmuki, P.; Silva, T. M.; Montemor, M. F. On the Supercapacitive Behaviour of Anodic Porous WO3-Based Negative Electrodes. *Electrochim. Acta* **2017**, *232*, 192−201.
(77) Zheng, F.; Wang, J.; Liu, W.; Zhou, J.; Li, H.; Yu, Y.; Hu, P.; Yan, W.; Liu, Y.; Li, R.; Zhen, Q.; Zhang, J. Novel Diverse-Structured h-WO3 Nanoflake Arrays as Electrode Materials for High Performance Supercapacitors. *Electrochim. Acta* **2020**, *334*, No. 135641.
(78) Xu, J.; Ding, T.; Wang, J.; Zhang, J.; Wang, S.; Chen, C.; Fang, Y.; Wu, Z.; Huo, K.; Dai, J. Tungsten Oxide Nanofibers Self-

Assembled Mesoscopic Microspheres as High-Performance Electrodes for Supercapacitor. *Electrochim. Acta* **2015**, *174*, 728−734.
(79) He, X.; Wang, X.; Sun, B.; Wan, J.; Wang, Y.; He, D.; Suo, H.; Zhao, C. Synthesis of Three-Dimensional Hierarchical Furball-like Tungsten Trioxide Microspheres for High Performance Supercapacitor Electrodes. *RSC Adv.* **2020**, *10* (23), 13437−13441.
(80) Zheng, F.; Gong, H.; Li, Z.; Yang, W.; Xu, J.; Hu, P.; Li, Y.; Gong, Y.; Zhen, Q. Tertiary Structure of Cactus-like WO3 Spheres Self-Assembled on Cu Foil for Supercapacitive Electrode Materials. *J. Alloys Compd.* **2017**, *712*, 345−354.
(81) Ji, S. H.; Chodankar, N. R.; Kim, D. H. Aqueous Asymmetric Supercapacitor Based on RuO2-WO3 Electrodes. *Electrochim. Acta* **2019**, *325*, No. 134879.
(82) Jia, J.; Liu, X.; Mi, R.; Liu, N.; Xiong, Z.; Yuan, L.; Wang, C.; Sheng, G.; Cao, L.; Zhou, X.; Liu, X. Self-Assembled Pancake-like Hexagonal Tungsten Oxide with Ordered Mesopores for Supercapacitors. *J. Mater. Chem. A* **2018**, *6* (31), 15330−15339.
(83) Lichchhavi; Lee, H.; Ohshita, Y.; Singh, A. K.; Shirage, P. M. Transformation of Battery to High Performance Pseudocapacitor by the Hybridization of W 18 O 49 with RuO 2 Nanostructures. *Langmuir* **2021**, *37*, 1141−1151, DOI: 10.1021/acs.langmuir.0c03056.
(84) Shembade, U. V.; Dhas, S. D.; Gurav, S. R.; Sonkawade, R. G.; Wategaonkar, S. B.; Ghatage, S. R.; Gaikwad, M. A.; Kim, J. H.; Parale, V. G.; Park, H. H.; Moholkar, A. V. Acid Substitutions for WO3 Nanostructures Synthesis by the Hydrothermal Route and Its Effect on Physio-Chemical and Electrochemical Properties for Supercapacitors. *J. Energy Storage* **2023**, *72*, No. 108432.
(85) Bhojane, P.; Shirage, P. M. Facile Preparation of Hexagonal WO3 Nanopillars and Its Reduced Graphene Oxide Nanocomposites for High-Performance Supercapacitor. *J. Energy Storage* **2022**, *55*, No. 105649.

https://doi.org/10.1021/acsomega.3c05677
ACS Omega 2023, 8, 40878−40889